







Engineering nitrogen- and hydrogen-related defects in ZnO nanowires using thermal annealingJosé Villafuerte ^{1,2}, Odette Chaix-Pluchery ¹, Joseph Kioseoglou ³, Fabrice Donatini,² Eirini Sarigiannidou ¹, Julien Pernot ^{2,*} and Vincent Consonni ^{1,†}¹Université Grenoble Alpes, CNRS, Grenoble INP, LMGP, F-38000 Grenoble, France²Université Grenoble Alpes, CNRS, Grenoble INP, Institut NEEL, F-38000 Grenoble, France³Physics Department, Aristotle University of Thessaloniki, 54124 Thessaloniki, Greece

(Received 16 December 2020; revised 24 March 2021; accepted 12 April 2021; published 6 May 2021)

The chemical bath deposition (CBD) of ZnO nanowires (NWs) is of high interest, but their formation occurs in a growth medium containing many impurities including carbon, nitrogen, and hydrogen, rendering the accurate determination of predominant crystal defects as highly debated. In addition to the typical interstitial hydrogen in bond-centered sites (H_{BC}) and zinc vacancy-hydrogen ($V_{Zn}-nH$) complexes, we reveal that nitrogen-related defects play a significant role on the physical properties of unintentionally doped ZnO NWs. We show by density functional theory that the $V_{Zn}-N_O-H$ defect complex acts as a deep acceptor with a relatively low formation energy and exhibits a prominent Raman line at 3078 cm^{-1} along with a red-orange emission energy of $\sim 1.82\text{ eV}$ in cathodoluminescence spectroscopy. The nature and concentration of the nitrogen- and hydrogen-related defects are found to be tunable using thermal annealing under oxygen atmosphere, but a rather complex, fine evolution including successive formation and dissociation processes is highlighted as a function of annealing temperature. ZnO NWs annealed at the moderate temperature of $300\text{ }^\circ\text{C}$ specifically exhibit one of the smallest free charge carrier densities of $5.6 \times 10^{17}\text{ cm}^{-3}$ along with a high mobility of $\sim 60\text{ cm}^2/\text{Vs}$ following the analysis of longitudinal optical phonon-plasmon coupling. These findings report a comprehensive diagram showing the complex interplay of each nitrogen- and hydrogen-related defect during thermal annealing and its dependence on annealing temperature. They further reveal that the engineering of the nitrogen- and hydrogen-related defects as the major source of crystal defects in ZnO NWs grown by CBD is capital to precisely control their electronic structure properties governing their electrical and optical properties in any devices.

DOI: [10.1103/PhysRevMaterials.5.056001](https://doi.org/10.1103/PhysRevMaterials.5.056001)**I. INTRODUCTION**

The optimization and control of the electrical and optical properties of ZnO nanowires (NWs) grown by the widely used low-temperature chemical bath deposition (CBD) technique are critical issues for enhancing the performances of the related piezoelectric [1,2], piezotronic [3], optoelectronic [4], photovoltaic [5], and chemical and/or biological sensor [6] devices. Accurate knowledge on the nature and concentration of intrinsic-extrinsic point defects governing the electronic structure properties of ZnO NWs is required. In the CBD technique [7], an inherent characteristic originates from the crystallization process of ZnO NWs operating in an aqueous solution, namely, in a hydrogen-rich environment [8–10]. Over the last years, the predominant role of hydrogen in unintentionally doped ZnO NWs grown by CBD has been supported by several chemical, optical, and electrical analyses [11–14]. The presence of hydrogen in the center of ZnO NWs has been detected by nuclear magnetic resonance [11] and elastic recoil detection analysis [12]. The correlated high density of free charge carriers in ZnO NWs has been shown by terahertz spectroscopy [15], scanning probe microscopy [16],

field-effect transistor (FET) measurements [17], scanning capacitance microscopy [18], and four-point probe resistivity measurements [13,14]. O- and Zn-polar ZnO nanorods grown by CBD within the selective area growth approach were further found to exhibit, on average, a high electrical conductivity of 10.2 and 90.9 S/cm, respectively [13]. Later, ZnO NWs grown by CBD within the spontaneous growth approach were also shown to present, on average, a high electrical conductivity ranging from 35.2 to 243.1 S/cm [14]. These statistical studies have revealed that the high density of free charge carriers in the range of 6.4×10^{17} to $1.1 \times 10^{19}\text{ cm}^{-3}$ for selective-area-grown ZnO nanorods and 2.7×10^{18} to $3.1 \times 10^{19}\text{ cm}^{-3}$ for spontaneously grown ZnO NWs is directly attributed to the massive incorporation of hydrogen by using Raman and cathodoluminescence spectroscopy [13,14].

For almost two decades, hydrogen-related defects in ZnO have been addressed by the pioneering work of Van de Walle [19], revealing from density functional theory (DFT) calculations that interstitial hydrogen (H_i) does not act as an amphoteric impurity as in many other semiconductors but as a shallow donor over the expected range of the Fermi level. Substitutional hydrogen on the oxygen lattice site (H_O) [20] and zinc vacancy-hydrogen ($V_{Zn}-nH$) defect complexes, where n lying in the range of 1–4 represents the number of involved H_i atoms [21,22], have further been considered to play a major role. Experimental evidence of the presence of

*Corresponding author: julien.pernot@neel.cnrs.fr†Corresponding author: vincent.consonni@grenoble-inp.fr

these hydrogen-related defects in ZnO thin films has been pointed out using optical spectroscopy [23–27]. H_i in the bond-centered site (H_{BC}) was previously considered as the most stable configuration [19], but a recent study has shown that the V_{Zn} -3H defect complex presents an even lower formation energy [14]. Hence, H_{BC} and the V_{Zn} -3H defect complex acting as two shallow donors with a very low formation energy along with H_O have been identified as the major source of n -type conductivity in unintentionally doped ZnO NWs grown by CBD [13,14].

In the field of piezoelectric devices [1], unintentionally doped ZnO NWs grown by CBD face the critical challenge of piezoelectric potential screening originating from the high density of free charge carriers in their center [28–31]. Under mechanical stress, a piezoelectric potential is generated along the polar c axis of ZnO NWs from the displacement of the charge centers of anions and cations. For a high concentration of shallow donors, a screening potential created from mobile free electrons is generated in the opposite direction, reducing in turn the overall magnitude of the piezoelectric potential [28]. Through analytical and finite element method simulations, the piezoelectric potential has been found to be strongly reduced as the concentration of shallow donors is increased above 10^{17} cm^{-3} [29–31]. The control of the concentration of shallow donors was thus shown to drastically improve the performance of sound-driven piezoelectric nanogenerators [32]. Additionally, surface Fermi level pinning was theoretically found to compensate for the detrimental effects of the high concentration of shallow donors by depleting the center of ZnO NWs but only to a limited extent for a high doping level [33]. As a result, the engineering of hydrogen-related defects (i.e., in terms of nature and concentration) in unintentionally doped ZnO NWs grown by CBD is of high significance. A typical strategy has involved a postdeposition thermal annealing to dissociate hydrogen-related defects and exodiffuse hydrogen from the bulk of ZnO thin films [34] and NWs [35,36]. Huang *et al.* [35] showed that a thermal annealing in air can drastically improve the intensity of the near-band edge (NBE) emission in the photoluminescence spectra of ZnO NWs grown by CBD. Urgessa *et al.* [36] investigated the stability of the I_4 line assigned to H_O in ZnO NWs grown by CBD as a function of annealing temperature. The present approach offers a great opportunity to monitor the nature and concentration of hydrogen-related defects in ZnO NWs, but it has not been explored yet in detail. More recently, the alternative oxygen plasma treatment in ZnO nanorods has also been found to improve the Schottky contact with Au on their top c -plane faces through the strong effects on the nature and concentration of hydrogen-related defects [37]. Furthermore, the growth medium contains hydrogen but also carbon and nitrogen species. The involvement of hydrogen, carbon, and nitrogen in the same medium is expected to play a significant role as well, for instance, by forming additional nitrogen- and hydrogen-based defect complexes [38–41]. However, the nature of these defect complexes and their assignment by using Raman and cathodoluminescence spectroscopy still need to be clarified, specifically in the context of CBD-grown ZnO NWs.

In this paper, the engineering of nitrogen- and hydrogen-related defects is performed by thermal annealing, where a series of isochronally annealed ZnO NWs spontaneously

grown by CBD are prepared under oxygen atmosphere in the temperature range of 200–1000 °C. The combination of Raman and cathodoluminescence spectroscopy with DFT calculations offers a comprehensive analysis of the evolution of these defects during the annealing process. It also shows the interplay between the nitrogen and hydrogen species in unintentionally doped ZnO NWs grown by CBD, which should be monitored to tune their electrical and optical properties.

II. EXPERIMENTAL AND THEORETICAL METHODS

A. Synthesis and thermal annealing of ZnO NWs

(001) silicon substrates were cleaned in an ultrasonic bath using acetone and isopropyl alcohol to remove the residual contaminants. The polycrystalline ZnO seed layers were deposited by dip coating using a sol-gel process. The chemical precursor solution consisted of 375 mM zinc acetate dihydrate [$\text{Zn}(\text{CH}_3\text{COO})_2 \cdot 2\text{H}_2\text{O}$, Sigma-Aldrich] and 375 mM monoethanolamine (Sigma-Aldrich) mixed in pure ethanol. It was stirred for several hours at 60 °C on a hot plate to obtain a clear solution and then at room temperature to complete the $\text{Zn}(\text{CH}_3\text{COO})_2$ dilution. The substrates were subsequently dipped into the solution and gently pulled out under a controlled atmosphere (<15% hygrometry). They were annealed for 10 min at 300 °C on a hot plate for the evaporation of residual organic compounds and for 1 h at 500 °C in an oven under air for the crystallization of ZnO seed layers. ZnO NWs were grown by CBD in a sealed reactor containing a chemical precursor solution of 30 mM zinc nitrate hexahydrate [$\text{Zn}(\text{NO}_3)_2 \cdot 6\text{H}_2\text{O}$, Sigma-Aldrich] and hexamethylenetetramine (HMTA, Sigma-Aldrich) mixed in deionized water. The sealed reactor was placed for 5 h in an oven kept at 85 °C. The pH value of ~ 5.5 was measured during the CBD process. Thermal annealing treatments were eventually performed in a tubular furnace under oxygen atmosphere for 1 h in the temperature range of 200–1000 °C.

B. Characterization techniques

The morphology of ZnO NWs was assessed by field-emission scanning electron microscopy (FESEM) imaging using a FEI Quanta 250 FESEM instrument. The nature and concentration of hydrogen-related defects were investigated by Raman and cathodoluminescence spectroscopy. Raman spectroscopy of ZnO NWs was achieved with a Horiba/Jobin Yvon Labram spectrometer equipped with a liquid nitrogen-cooled charge-coupled device (CCD) detector. An Ar^+ laser exhibiting a 514.5 nm line and a power on the sample surface $\sim 0.64 \text{ mW}$ was focused to a spot size $\sim 1 \mu\text{m}^2$ using a 100 \times objective. The integration time depended on the spectral region and ranged from 2 min for low wavenumbers corresponding to the ZnO-related typical phonon modes to 1 h for high wavenumbers corresponding to the nitrogen- and hydrogen-related phonon modes. The spectrum calibration was performed at room temperature using a silicon reference sample. The theoretical position of the silicon Raman line was set to 520.7 cm^{-1} . Here, 5 K cathodoluminescence measurements were performed on single ZnO NWs dispersed on SiO_2/Si substrates with a FEI Inspect F50 FESEM instrument equipped with a liquid helium-cooled stage. The

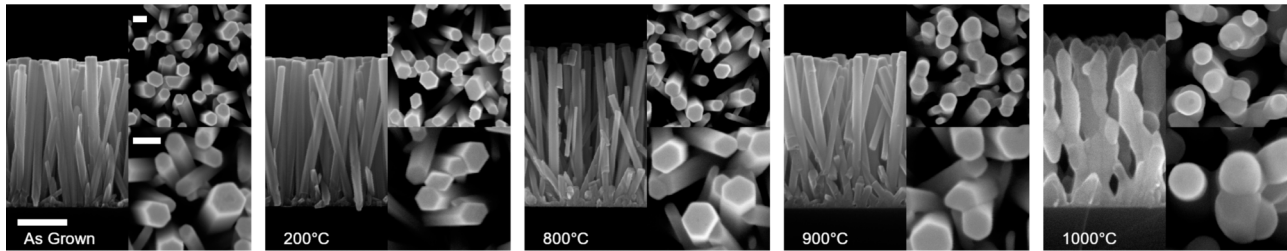


FIG. 1. Cross-sectional and top-view field-emission scanning electron microscopy (FESEM) images of unintentionally doped ZnO NWs grown by chemical bath deposition (CBD) and annealed for 1 h under oxygen atmosphere in the temperature range of 200 to 1000 °C. The scale bars correspond to 500 and 100 nm for the cross-sectional and top views, respectively.

cathodoluminescence signal was collected through a parabolic mirror and analyzed with a 550 mm focal length monochromator equipped with 600 grooves/mm diffraction grating. Cathodoluminescence spectra were recorded with a thermoelectric cooled silicon CCD detector. A low acceleration voltage of 5 kV and a small spot size (i.e., <10 nm) were used to focus the acquisition on the single ZnO NW.

C. DFT Method

The study about the wurtzite structure of ZnO and of the related point defects was carried out using the VASP code with projector-augmented wave (PAW) potentials [42,43] under the Perdew-Burke-Ernzerhof derivation of the generalized gradient approximation (GGA-PBE) [44,45] of the DFT. A Monkhorst-Pack mesh of $8 \times 8 \times 6$ for the $1 \times 1 \times 1$ unit cell was set to define the reciprocal-space resolution corresponding to the k -point mesh generation. The k -point mesh was Γ -centered, and the cutoff energy was set to 600 eV. A $4 \times 4 \times 3$ supercell composed of 192 atoms was used to ensure the structural relaxation and the accurate calculations of the optoelectronic properties of point defects in ZnO. Extensive tests concluded that these properties cannot be accurately determined in smaller sized supercells. The convergence with respect to k -point sampling, slab, and vacuum thickness was explicitly checked. The DFT + U method was selected to accurately calculate the electronic structure and optical properties, as a computational cost-efficient method in large-sized supercells [46]. The values of the Hubbard parameters U were incorporated for the d states of Zn ($U_{d,Zn}$) and p states of O ($U_{p,O}$) to produce good lattice constants and band gap energy of 3.4 eV for ZnO [47]. The following U values were taken [48]: $U_{d,Zn} = 10.5$ eV and $U_{p,O} = 7.0$ eV. The application of self-consistent values of U produces electronic structures that are in better agreement with hybrid functional calculations, as well as almost universally in better agreement with the experimental lattice geometry [49]. The s states of H were treated at the PBE level, which is a common approach for these atoms. The p states of N were introduced using the same U value as the p states of O: $U_{p,N} = 7.0$ eV. The present assumption considering $U_{p,N} = U_{p,O}$ as reported in Refs. [46,50,51] is realistic and consistent due to the fact that N atoms substitute for O atoms in the ZnO lattice. The oxygen chemical potential μ_O was set to -2.11 eV, corresponding to intermediate growth conditions. The formation energies of each point defect complex were computed using the well-established formalisms described in Ref. [52], whose main

expression was given in Ref. [14]. The luminescence positions of the $V_{Zn}-N_O-H$ defect complex were calculated for the different transition levels within the Franck-Condon approximation using the effective one-dimensional configuration coordinate to get the zero phonon line energy (E_{ZPL}), emission energy (E_{emission}), and absorption energy ($E_{\text{absorption}}$), as presented in Refs. [14,53,54].

III. RESULTS AND DISCUSSION

A. Morphological properties of as-grown and annealed ZnO NWs

The CBD of unintentionally doped ZnO NWs on a c -axis oriented polycrystalline ZnO seed layer deposited by dip coating on silicon was performed at 85 °C and at a pH value of ~ 5.5 using $Zn(NO_3)_2$ and HMTA [55,56]. The as-grown ZnO NWs were annealed for 1 h in a tubular furnace under oxygen atmosphere in the temperature range of 200–1000 °C. The morphology of as-grown and annealed ZnO NWs is presented in Fig. 1 by FESEM imaging. Before the thermal annealing, as-grown ZnO NWs are vertically aligned with a hexagonal shape that is typical of their wurtzite structure along the polar c axis [57]. They exhibit a mean diameter and length of 100 ± 27 and 1560 ± 71 nm, respectively [14]. In the annealing temperature range of 200–800 °C, no change of the morphology of ZnO NWs is shown, indicating their morphological stability as expected from the high melting point of ZnO ~ 2248 K [58]. As the annealing temperature is raised to 900 °C, ZnO NWs start to coalesce to a larger extent, and their hexagonal shape is less pronounced. At an annealing temperature of 1000 °C, ZnO NWs have a wavy structure, and their hexagonal shape is completely lost at the benefit of a cylinder shape. From 900 °C, ZnO thin films and NWs typically undergo recrystallization phenomena through diffusive transport process, leading to a structural reordering that was previously used to transform ZnO thin films into NW arrays [59].

B. Raman spectroscopy of as-grown and annealed ZnO NWs

The Raman scattering spectra of as-grown and annealed ZnO NWs are presented in Fig. 2 with a zoom-in to the area of interest in Fig. S1 in the Supplemental Material [60]. In the low-wavenumber range of 50–900 cm^{-1} , the optical phonon modes observed in as-grown NWs are located at 99 (E_2^{low}), 378 [$A_1(\text{TO})$], 438 (E_2^{high}), and 574 [$A_1(\text{LO})$] cm^{-1} , showing the wurtzite structure of ZnO NWs [61]. Second-order

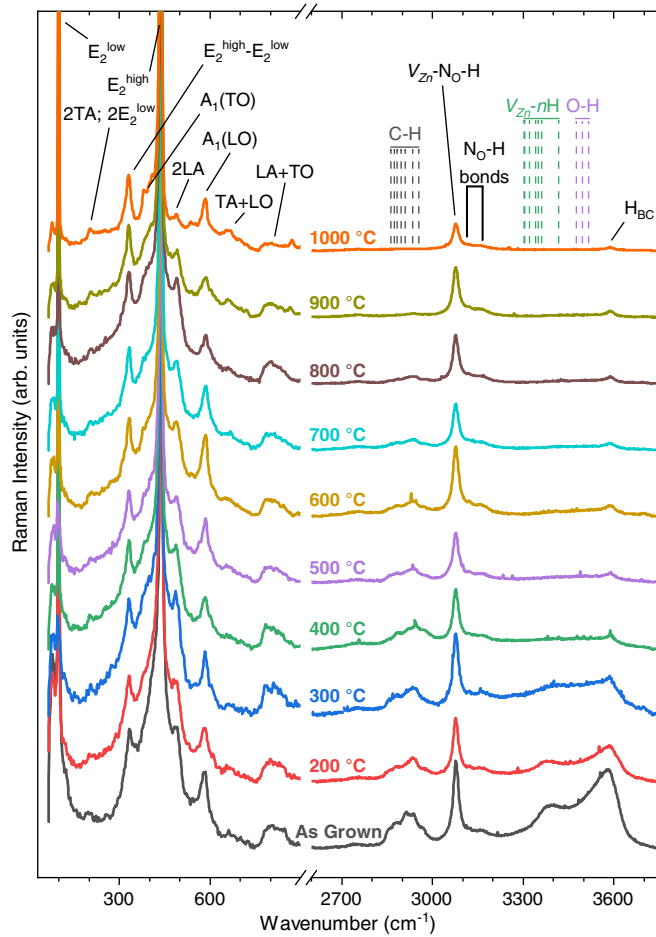


FIG. 2. Raman spectra of unintentionally doped ZnO NWs grown by chemical bath deposition (CBD) and annealed for 1 h under oxygen atmosphere in the temperature range of 200 to 1000 °C. The insets delimit the calculated and experimental vibrational frequencies from Raman and infrared absorption spectroscopy as deduced from Refs. [14,24,53,70,75,76].

Raman lines occur at 203 (2TA/2E₂^{low}), 483 (2LA), 666 (TA + LO), and 812 (LA + TO) cm⁻¹. The Raman line at 333 cm⁻¹ corresponds to the E₂^{high} - E₂^{low} mode, but the involvement of the 1s → 2p donor state transition assigned to H_{BC} may also take place [25]. No additional modes related to residual extrinsic impurities including aluminum, gallium, iron, and antimony are detected [62]. The low value of pH ~5.5 along with the absence of chemical additives including these dopants exclude the significant incorporation of residual extrinsic impurities [63,64] other than hydrogen, carbon, and nitrogen present in the chemical precursors and growth medium. Nevertheless, no additional mode related to nitrogen substituting for the oxygen lattice site (N_O) is detected either [65]. As the annealing temperature is raised from 200 to 1000 °C, the nature of the optical phonon modes does not differ. However, the significant increase in the intensity of the E₂^{high} mode along with the decrease in its full width at half maximum (FWHM) from 17.5 to 10.1 cm⁻¹, as seen in Fig. S2 in the Supplemental Material [60], highlight an improvement of the crystallinity of annealed ZnO NWs through restoring and recrystallization phenomena. Correlatively, the line

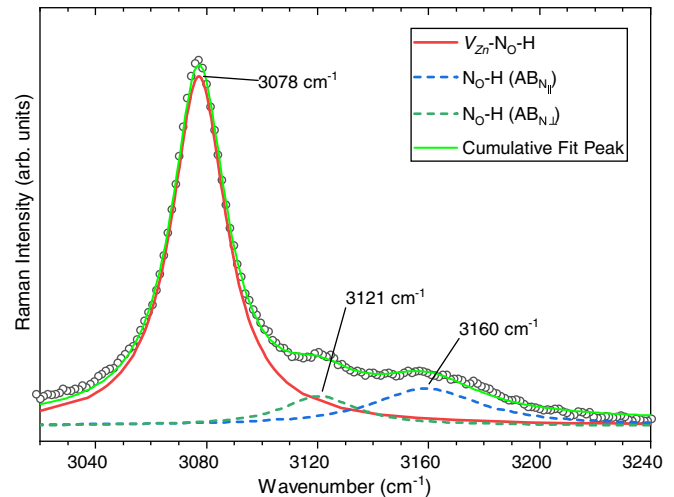


FIG. 3. Zoom-in of the area of interest corresponding to the Raman lines assigned to the nitrogen-related defects in ZnO NWs grown by chemical bath deposition (CBD) and annealed for 1 h under oxygen atmosphere at 600 °C. The three Raman lines assigned to nitrogen-related defects are fitted by Lorentzian functions to decouple their contribution to the experimental data.

position of the E₂^{high} mode shifts toward lower wavenumbers until its stabilization at ~437.6 cm⁻¹, indicating a possible relaxation of the wurtzite structure of ZnO NWs.

In the high-wavenumber range of 2750–3750 cm⁻¹, many Raman lines are associated with the presence of hydrogen, carbon, and nitrogen. From 2750 to 3000 cm⁻¹, several sharp Raman lines at 2890, 2918, 2948, and 2988 cm⁻¹ are attributed to the antisymmetric and symmetric stretching bonds of C-H_x groups (x = 1, 2, 3) [38], originating from the residual HMTA molecules adsorbed on the nonpolar *m*-plane sidewalls of ZnO NWs [56,66,67]. Carbon-related species are thus detected only on the surfaces of ZnO NWs. A prominent Raman line at 3078 cm⁻¹ with a FWHM of 24.1 cm⁻¹ along with two weak lines at 3121 and 3160 cm⁻¹ also occur as shown in Fig. 3 and typically lie in the wavenumber range where the phonon modes are associated with nitrogen-related bonds [38–41,68]. Nickel and Fleischer [38] identified a Raman line at 3096 cm⁻¹ tentatively assigned to the stretching vibration of the N_O-H bonds. Li *et al.* [39] showed the presence of a line at a wavenumber of 3020 cm⁻¹ using infrared absorption spectroscopy. From DFT calculation, they revealed that N_O⁻ and H_i⁺ have a high probability of forming a neutral N_O-H defect complex in the antibonding configuration both in perpendicular (AB_{N⊥}) and parallel (AB_{N||}) positions, exhibiting the lowest formation energies. Depending on the pseudopotentials used, two respective infrared modes with a corresponding line at 3055/3117 cm⁻¹ and 3084 cm⁻¹ were calculated. Also, the breaking of the N_O-H bonds requires an energy >1.25 eV, highlighting its high stability [68]. Correlatively, Jokela and McCluskey [40,41] unambiguously identified a N_O-H bond-related phonon mode giving rise to a line at 3150.6 cm⁻¹ using infrared absorption spectroscopy. Kumar *et al.* [69] correspondingly showed the presence of the same line ~3150 cm⁻¹ using Raman spectroscopy. From these theoretical and experimental investigations, the Raman lines at 3121 and 3160 cm⁻¹

separated by $\sim 40\text{ cm}^{-1}$ are attributed to the N_O -H bonds in the $\text{AB}_{\text{N}\perp}$ and $\text{AB}_{\text{N}\parallel}$ configurations, respectively. These N_O -H bonds are located on the surfaces of ZnO NWs when originating from the residual HMTA molecules [56] and in their center via the related N_O -H defect complex. More importantly, a Raman line at 3078 cm^{-1} was assigned to the $\text{V}_{\text{Zn}}\text{-N}_\text{O}$ -H defect complex as a presumably single shallow acceptor with an ionization energy of 134 meV [70], stabilizing the $\text{V}_{\text{Zn}}\text{-N}_\text{O}$ defect complex [71]. The line position of the $\text{V}_{\text{Zn}}\text{-N}_\text{O}$ -H defect complex perfectly fits our line in the present Raman spectra. The nature of this defect complex is, however, highly debated, as recent DFT calculations have reported its deep [72] or shallow [73] acceptor character. Consequently, it turns out that our prominent Raman line pointing at 3078 cm^{-1} is attributed to the $\text{V}_{\text{Zn}}\text{-N}_\text{O}$ -H defect complex presumably located on the surfaces of ZnO NWs and in their center. During the CBD process, the solubilization of $\text{Zn}(\text{NO}_3)_2$ in aqueous solution results in the formation of Zn^{2+} and NO_3^- ions, which may be favorable for the incorporation of a significant amount of nitrogen in the center of ZnO NWs. From 3200 to 3750 cm^{-1} , several additional Raman lines related to hydrogen in different forms and located on the surfaces and in the center of ZnO NWs take place. An asymmetric broad Raman band centered at 3575 cm^{-1} involves a dominant Raman line assigned to H_{BC} [24,74] and a shoulder $\sim 3500\text{ cm}^{-1}$ attributed to O-H bonds [24,70,75] on the surfaces of ZnO NWs. Another asymmetric broad Raman band centered $\sim 3375\text{ cm}^{-1}$ involves the contribution of $\text{V}_{\text{Zn}}\text{-nH}$ defect complexes in the wavenumber range of $3300\text{--}3418\text{ cm}^{-1}$, mainly $\text{V}_{\text{Zn}}\text{-H}$ [24,53], $\text{V}_{\text{Zn}}\text{-2H}$ [24], and $\text{V}_{\text{Zn}}\text{-3H}$ [76] defect complexes.

Following the assignment of all the Raman lines attributed to nitrogen- and hydrogen-related defects, the Raman spectra were normalized with respect to the line assigned to the E_2^{high} mode, and the relative intensity of each line was determined by fitting its area by a Lorentzian function. The evolution of the relative intensity of the Raman lines attributed to nitrogen- and hydrogen-related defects with the annealing temperature is presented in logarithmic scale in Fig. 4. At the annealing temperature of 200°C , a strong decrease in the relative intensity of $\sim 50\%$ is shown for both Raman lines assigned to H_{BC} and $\text{V}_{\text{Zn}}\text{-nH}$ defect complexes, with a significant steady decrease in the annealing temperature range of $400\text{--}1000^\circ\text{C}$. At the annealing temperatures of 300 and 600°C , an increase in the relative intensity of both Raman lines assigned to H_{BC} and $\text{V}_{\text{Zn}}\text{-nH}$ defect complexes is revealed. This increase is more pronounced for the Raman line ascribed to $\text{V}_{\text{Zn}}\text{-nH}$ defect complexes in ZnO NWs annealed at 300°C and for the Raman line attributed to H_{BC} in ZnO NWs annealed at 600°C . This specific behavior was previously reported partly by Koch *et al.* [34], showing that H_{BC} forms electrically inactive interstitial hydrogen molecules (H_2) after a thermal annealing at low temperature. The further increase in the annealing temperature makes H_{BC} energetically favorable as compared with H_2 molecules, resulting in its dissociation and in the reappearance of H_{BC} with a maximum concentration in the range of $650\text{--}700^\circ\text{C}$ [34]. In our case, the formation of interstitial H_2 molecules at the expense of H_{BC} accounts for the sharp decrease in the relative intensity of this mode at the annealing temperature of 200°C . However, the further increase in the annealing temperature could make

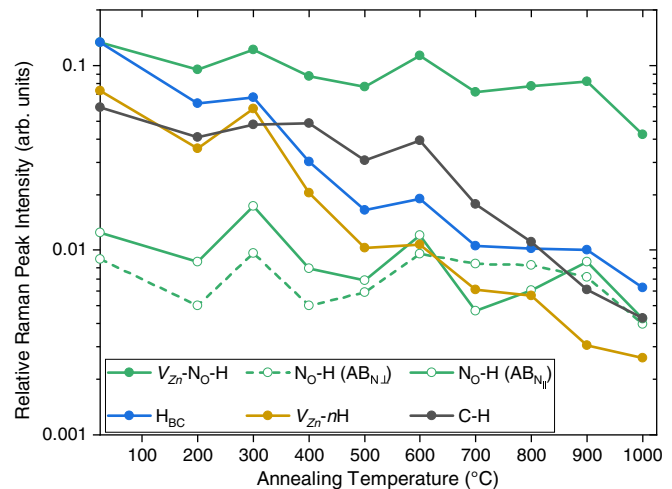


FIG. 4. Evolution of the relative intensity of the Raman lines assigned to hydrogen-related defects of unintentionally doped ZnO NWs grown by chemical bath deposition (CBD) and annealed for 1 h under oxygen atmosphere in the temperature range of 200 to 1000°C . The first data point is related to as-grown ZnO NWs.

energetically favorable the formation of not only H_{BC} but also other hydrogen-related defects such as C-H_x , $\text{V}_{\text{Zn}}\text{-nH}$, N_O -H, and $\text{V}_{\text{Zn}}\text{-N}_\text{O}$ -H defect complexes, hence explaining the sharp increase of the Raman lines related to these defects at the annealing temperatures of 300 and 600°C . The Raman lines assigned to N_O -H bonds and the $\text{V}_{\text{Zn}}\text{-N}_\text{O}$ -H defect complex present a greater stability since only a 30% decrease in their relative intensity is shown in ZnO NWs annealed at 200°C together with a small variation up to the annealing temperatures of $800\text{--}900^\circ\text{C}$ [70]. The evolution of the relative intensities of the N_O -H bonds in $\text{AB}_{\text{N}\parallel}$ configuration and of the $\text{V}_{\text{Zn}}\text{-N}_\text{O}$ -H defect complex is very similar, whereas the evolution of the relative intensity of the N_O -H bonds in $\text{AB}_{\text{N}\perp}$ configuration significantly differs in the annealing temperature range of $700\text{--}900^\circ\text{C}$. Gao *et al.* [77,78] stated that the thermal annealing of nitrogen-doped ZnO NWs under oxygen atmosphere at temperatures above 500°C promotes the exodiffusion of N_O via an oxygen vacancy-assisted mechanism, as supported by DFT calculations. However, this diffusion mechanism is expected to occur gradually, since N_O is systematically compensated by H_i , and residual amounts of N_O -H and the $\text{V}_{\text{Zn}}\text{-N}_\text{O}$ -H defect complex have been shown up to an annealing temperature of 800°C [70,77], which is even higher here and $\sim 1000^\circ\text{C}$. Hence, an interplay between the contributions from both defects with a different thermal stability is expected to account for the evolution of the present Raman lines. It should also be noted that, at the annealing temperature of 1000°C , the Raman lines attributed to N_O -H bonds and the $\text{V}_{\text{Zn}}\text{-N}_\text{O}$ -H defect complex and, followed by H_{BC} , present the most prominent intensities for the nitrogen- and hydrogen-related defects. The relative thermal stability of the C-H_x bonds also confirms that they are trapped on the m -plane sidewalls of ZnO NWs, hence requiring high annealing temperatures for activating efficient desorption phenomena starting at the annealing temperature of 700°C .

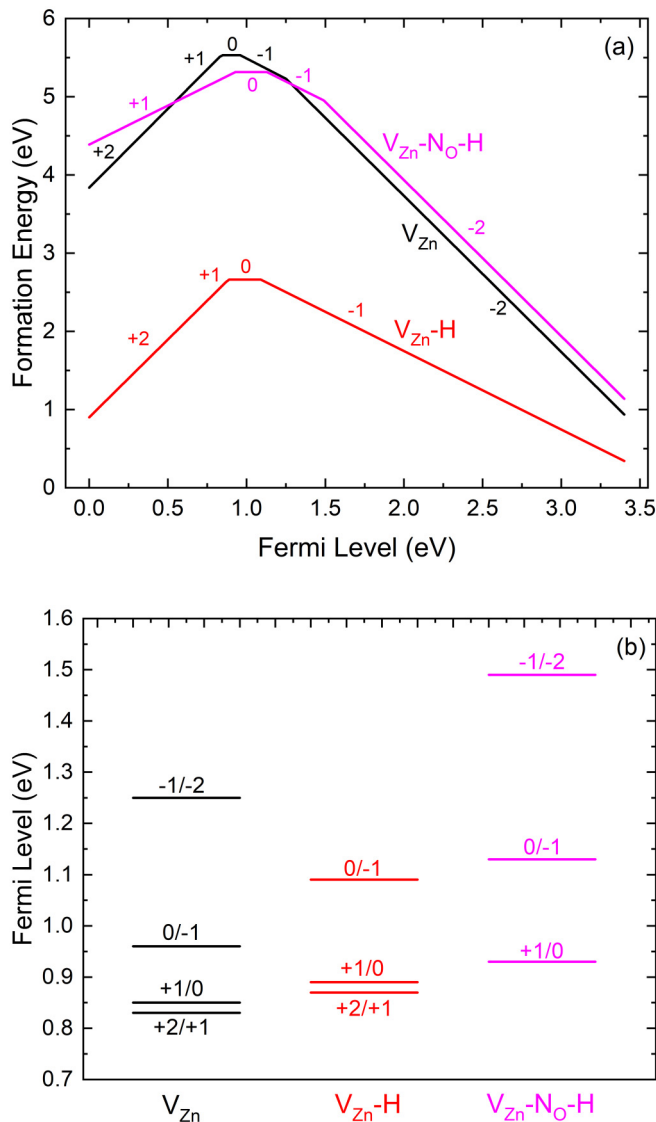


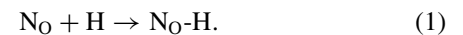
FIG. 5. (a) Formation energies of nitrogen- and hydrogen-related defects in ZnO as a function of the Fermi level determined by density functional theory (DFT) calculations. The most stable configuration with the lowest energy is presented for each charge state. The zero of Fermi energy was set at the valence band maximum. Chemical potential values of $\mu_O = -2.11$ eV and $\mu_H = -0.475$ eV were employed. (b) Transition levels of each of V_{Zn} , $V_{Zn}-H$, and $V_{Zn}-N_O-H$ defects as a function of the vertically aligned Fermi level.

C. Structure of crystal defects using DFT

The role of the $V_{Zn}-N_O-H$ defect complex in ZnO was carefully investigated by DFT calculations in the same conditions as in Ref. [14], using the VASP code with PAW potentials [42,43] under the GGA-PBE [44,45]. The formation energy of the $V_{Zn}-N_O-H$ defect complex as a function of the Fermi level is presented in Fig. 5(a) along with the formation energies of V_{Zn} and the $V_{Zn}-H$ defect complex for direct comparison. The transition levels of the different thermodynamic charge states of V_{Zn} , $V_{Zn}-H$, and $V_{Zn}-N_O-H$ defect complexes are gathered in Fig. 5(b).

As reported in several investigations using DFT calculations [14,53,54] and in Fig. 5(a), V_{Zn} and the $V_{Zn}-H$ defect

complex act as deep acceptors with a -2 and -1 charge state, respectively, when the Fermi level is close to the conduction band minimum. The formation energy of the $V_{Zn}-H$ defect complex is smaller than the formation energy of V_{Zn} for intermediate conditions, showing its efficient passivation by one H_i atom. The addition of one or two H_i atoms to the $V_{Zn}-H$ defect complex results in the formation of stable $V_{Zn}-2H$ and $V_{Zn}-3H$ defect complexes, the latter being a shallow donor with the $+1$ charge state and exhibiting the lowest formation energy regardless of the Fermi level in the bandgap [14]. The addition of N_O in ZnO has been investigated in detail using DFT calculations [39,68,72,73]. N_O typically acts as a deep acceptor with a -1 charge state and a relatively large formation energy when the Fermi level is close to the conduction band minimum for intermediate and O-rich conditions [39]. In the ZnO NWs grown by CBD where the hydrogen concentration is large [14] and given that hydrogen has a low migration barrier in ZnO [79], the following reaction spontaneously occurs because the formation energy of the N_O-H defect is lower than the sum of the formation energies of the individual N_O and H species [39,68,73]:



The formation of N_O is thus unlikely in ZnO NWs grown by CBD at the benefit of the N_O-H defect complex, as revealed in the Raman spectra of Fig. 2, showing no additional modes related to N_O in the low-wavenumber range [65] but instead the occurrence of two lines associated with N_O-H bonds at 3121 and 3160 cm^{-1} [38]. It should further be noted that the formation of N_{Zn} is even less likely in the present conditions [71]. Additionally, in the ZnO NWs grown by CBD where the concentration of V_{Zn} is large [14], the following reaction spontaneously proceeds as well to form the $V_{Zn}-N_O-H$ defect complex [73]:



In contrast, the formation of the $V_{Zn}-N_O$ defect complex is unlikely when the hydrogen concentration is large. The formation energy of the $V_{Zn}-N_O-H$ defect complex lies in the same range as the formation energy of V_{Zn} and appears slightly larger than the one of the $V_{Zn}-H$ defect complex when the Fermi level is close to the conduction band minimum for intermediate conditions, as shown in Fig. 5(a). The $V_{Zn}-N_O-H$ defect complex acts as a deep acceptor with a -2 charge state, which agrees with the hybrid functionals study reported in Ref. [72]. The density of states (DOS) of the $V_{Zn}-N_O-H$ defect complex using the PyProcar Python package [80] is presented in Fig. S3 in the Supplemental Material [60]. The p states of O and N in the band gap are found to coincide, which is in accordance with the corresponding hybrid functionals study [53]. The $(-1/-2)$ transition level lies at 1.49 eV above the valence band maximum, as represented in Fig. 5(b). The stable atomic configurations of the $V_{Zn}-N_O-H$ defect complex in the relaxed wurtzite structure are presented in Fig. 6. To investigate the structural configurations of the $V_{Zn}-N_O-H$ defect complex, all the possible atomistic configurations have been considered taking into account the neutral, $+1$, -1 , and -2 charge states. Initially, the N atom was considered to substitute an O undercoordinated atom in one of the three basal neighboring positions of the V_{Zn} as well as the axial O

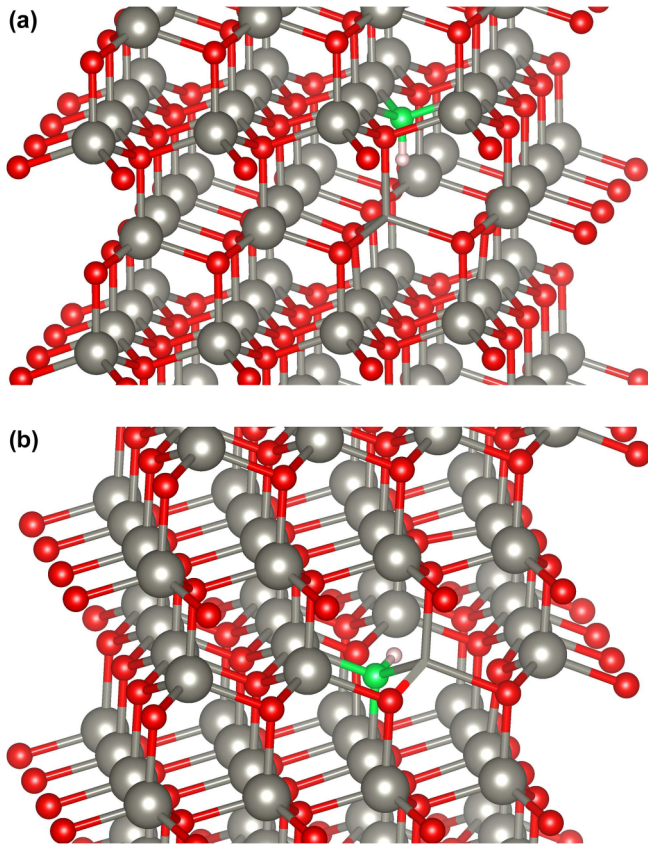


FIG. 6. Structural models for the most stable atomic configuration of the V_{Zn} - N_O -H defect complex. In (a), the axial V_{Zn} - N_O -H defect complex is represented. In (b), the basal V_{Zn} - N_O -H defect complex is represented. The axial configuration is found to be energetically favorable by 0.04 eV with respect to the basal one. Large gray balls, small red balls, small green balls, and small pink balls denote zinc, oxygen, nitrogen, and hydrogen atoms, respectively. The zinc atom in front of the V_{Zn} was taken out for the sake of clarity, and only its bonds with the neighboring oxygen atoms are represented.

undercoordinated atom. Moreover, the H atom was examined to be bonded with the N atom as well as with the rest of O undercoordinated atoms. In all cases, the energetically favorable H bond interaction is found to be the H-N by about 0.4–0.5 eV with respect to the H-O. On the other hand, the substitution of the axial O undercoordinated atom by an N atom is found to be energetically favorable with respect to the basal substitution by only 0.04 eV, for all examined charge states.

The luminescence positions of the V_{Zn} - N_O -H defect complex for the different transition levels are reported in Table I. In the expected thermodynamic charge state, the V_{Zn} - N_O -H defect complex notably exhibits an emission energy of 1.82 eV corresponding to the $(-1/-2)$ transition level.

D. Cathodoluminescence spectroscopy of as-grown and annealed ZnO NWs

The 5 K cathodoluminescence spectra of as-grown and annealed single ZnO NWs are presented in Fig. 7(a). The NBE emission of as-grown ZnO NWs is marked by the dominant contribution of radiative transitions involving neutral donor-bound A-excitons ($D^{\circ}X_A$) around 3.369 eV with a FWHM of 39.5 meV, as revealed in Figs. 7(b) and S4 in the Supplemental Material [60]. The involvement of the I_4 and I_5 lines at 3.3628 and 3.3614 eV assigned to H_O and the V_{Zn} -3H defect complex, respectively, proceeds in that energy range [14,25–27]. Additionally, H_{BC} involved in a line \sim 3.360 eV also contributes to the NBE emissions [14,25]. As the annealing temperature is increased up to 300 °C, a significant 6.7 meV redshift of the NBE emissions of annealed ZnO NWs is induced, as seen in Fig. S4 in the Supplemental Material [60]. At the annealing temperature of 500 °C, the NBE emission centered at 3.363 eV lies in the energy range of radiative transitions involving $D^{\circ}X_A$. However, its FWHM broadens to the highest value of 50.9 meV, suggesting an important contribution of radiative transitions involving neutral acceptor-bound A excitons ($A^{\circ}X_A$) [81]. At the annealing temperature of 600 °C, a prominent redshift of 15.2 meV centers the NBE emissions of annealed ZnO NWs at 3.354 eV, where radiative transitions involving $A^{\circ}X_A$ are mostly involved [81]. The increase in the contribution of $A^{\circ}X_A$ emissions very well correlates the highest V_{Zn} - N_O -H to H_{BC} relative intensity ratio from the corresponding Raman lines, as depicted in Fig. S5 in the Supplemental Material [60]. This might again indicate that the V_{Zn} - N_O defect complex [71] is more favorable for trapping the dissociated H_i atom [70] than a single V_{Zn} . Starting from 700 °C, the high crystalline quality of annealed ZnO NWs is inferred by the overall appearance of longitudinal optical (LO) phonon replicas separated from each other by a phonon energy of \sim 72 meV in ZnO [26]. The 3.289, 3.219, and 3.149 eV lines are associated with the first, second, and third LO phonon replicas of $D^{\circ}X_A$ transitions. The presence of the second order of the NBE emissions (2° NBE) also occurs at \sim 1.68 eV [82]. The spectra recorded on ZnO NWs annealed at 800 and 900 °C, to a smaller extent, contain a prominent shoulder \sim 3.31 eV, which has usually been related to $A^{\circ}X_A$ [83,84], donor-acceptor pair (DAP) [85–87], and free electron-to-acceptor (FA) [88] transitions in nitrogen-doped ZnO films and NWs. The line at 3.248 eV further represents the first LO phonon replica of the FA transitions (FA-1LO). The nature of the nitrogen-related defects involved in this line is, however, still under debate. The contribution of N_O can be excluded here as no related additional modes in the Raman spectra in Fig. 2 occur. More recently, Reynolds *et al.* [70] correlated the presence of this line related to FA transitions with the formation of the V_{Zn} - N_O -H defect complex. However,

TABLE I. Effective parameters for the computed luminescence transitions of the V_{Zn} - N_O -H defect complex.

	Transition level	$E_{\text{transition}}$ (eV)	E_{emission} (eV)	E_{ZPL} (eV)	$E_{\text{absorption}}$ (eV)
V_{Zn} - N_O -H	$\varepsilon(+1/0)$	0.93	2.50	2.47	2.67
	$\varepsilon(0/-1)$	1.13	2.27	2.27	2.63
	$\varepsilon(-1/-2)$	1.49	1.82	1.91	2.28

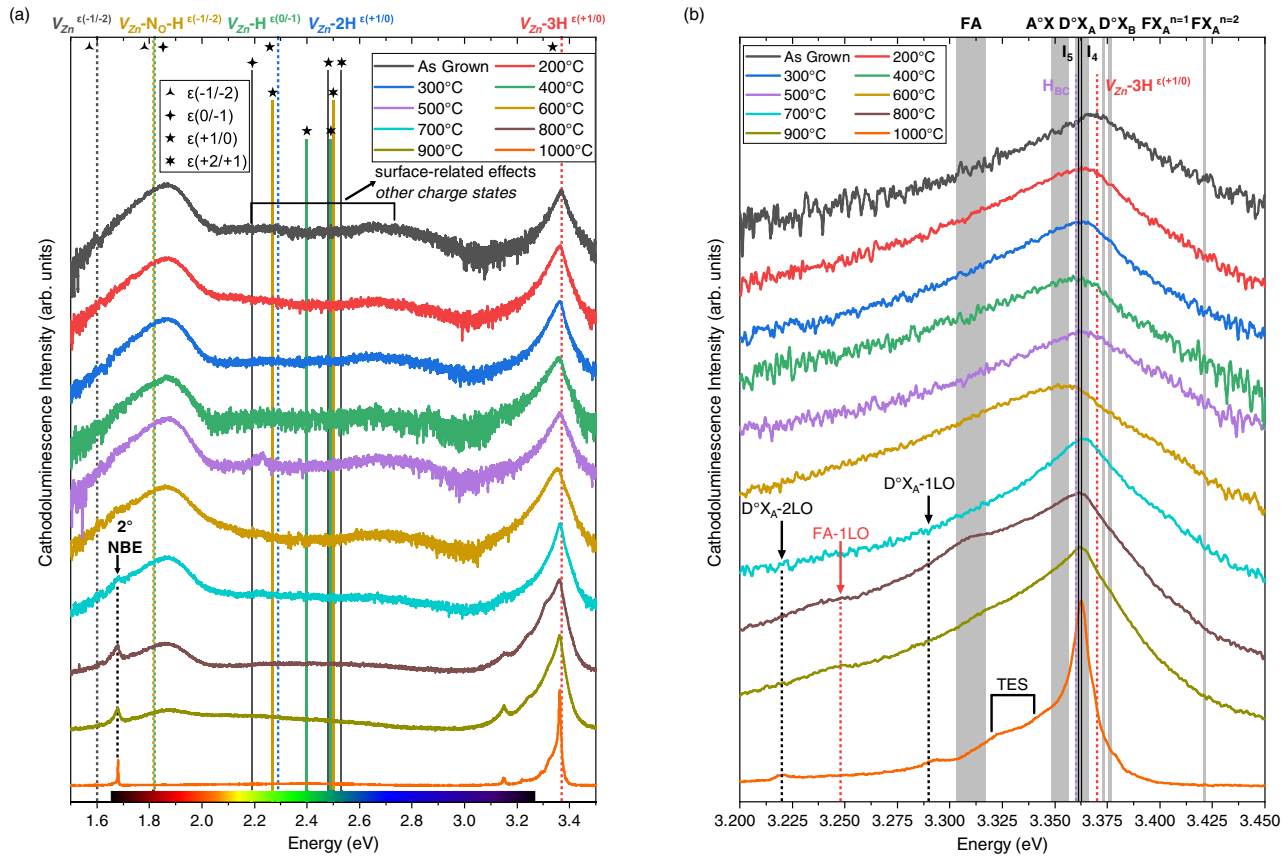


FIG. 7. (a) 5 K cathodoluminescence spectra of unintentionally doped single ZnO NWs grown by chemical bath deposition (CBD) and annealed for 1 h under oxygen atmosphere in the temperature range of 200 to 1000 °C. The insets represent the emission energy of transitions as inferred from density functional theory (DFT) calculations in this paper and in Refs. [14,53,54]. (b) Corresponding near-band edge (NBE) emission regions. The inset represents the emission energy of transitions as deduced from DFT calculations in this paper and from experimental data in Refs. [14,25,27].

this line does not occur in ZnO NWs annealed at a lower temperature, while the Raman line at 3078 cm^{-1} clearly takes place in Fig. 2, which somehow contradicts the present assignment to the $V_{\text{Zn}}\text{-N}_\text{O}\text{-H}$ defect complex. At the annealing temperatures of 900 and 1000 °C, the NBE emissions are considerably narrower and dominated by radiative transitions involving $\text{D}^\circ\text{X}_\text{A}$, where a drastic decrease in the FWHM from 39.5 down to 4.7 meV is shown in Fig. S4 in the Supplemental Material [60]. At the annealing temperature of 1000 °C, the FA transitions have vanished, suggesting the disappearance of the associated defects. At this high annealing temperature, the narrow line from the NBE emission is centered on the I_4 line and presents a shoulder located $\sim 3.33\text{ eV}$, originating from the corresponding two-electron satellite (TES) transitions [26]. As a result, both transitions show the predominance of residual H_O in ZnO NWs annealed at 1000 °C. Additionally, the presence of residual H_BC as revealed in Figs. 2–4 also contributes to the NBE emissions at this annealing temperature.

The emissions in the visible spectral region correspond to the dominant broad red-orange band centered at 1.86 eV and to the yellow-green band centered at 2.22 eV, which have been attributed to the $0/-1$ and $+1/0$ transition levels of the $V_{\text{Zn}}\text{-H}$ and $V_{\text{Zn}}\text{-2H}$ defect complexes formed in the bulk of ZnO NWs, respectively [14]. Interestingly, the red-orange emission band also involves the contribution of the $-1/-2$ transition level

of the $V_{\text{Zn}}\text{-N}_\text{O}\text{-H}$ defect complex with an emission energy of 1.82 eV, as reported in Table I. The red-orange emission band is thus related to two different deep acceptors (i.e., $V_{\text{Zn}}\text{-H}$ and $V_{\text{Zn}}\text{-N}_\text{O}\text{-H}$), but the decoupling of each contribution is not straightforward due to the proximity of both emission energies. The yellow-green emission band is instead related to the neutral $V_{\text{Zn}}\text{-2H}$ defect complex with no electrical activity [14]. An additional contribution from the $0/-1$ transition level of the $V_{\text{Zn}}\text{-N}_\text{O}\text{-H}$ defect complex located on the surfaces of ZnO NWs may proceed at 2.27 eV. The green-blue emission band centered at 2.68 eV is attributed to V_{Zn} as well as nitrogen- and hydrogen-related defects located on the surfaces of ZnO NWs, including $V_{\text{Zn}}\text{-H}$ [14], $V_{\text{Zn}}\text{-2H}$ [14], and $V_{\text{Zn}}\text{-N}_\text{O}\text{-H}$ defect complexes with the emission energies of $\sim 2.50\text{ eV}$ corresponding to the $+1/0$ transition level. These unexpected charge states in the transition levels of hydrogen-related defects are due to the generation of electron-hole pairs under electron beam excitation and to the further migration of holes toward the surfaces of ZnO NWs where they are highly concentrated owing to upward band-bending [14], which is related to the surface depletion region originating from the adsorbed oxygen ions [89].

Following the assignment of the radiative transitions to nitrogen- and hydrogen-related defects in the visible region of the electromagnetic spectrum, the relative intensity of each emission band was determined by fitting its area by a

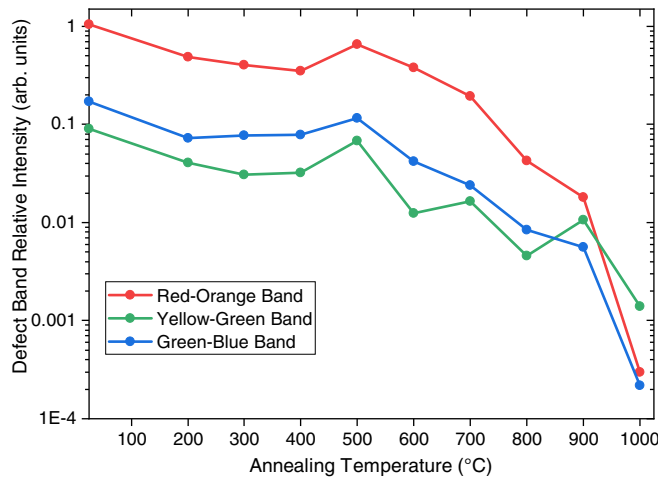


FIG. 8. Evolution of the relative intensity of 5 K cathodoluminescence spectrum bands in the visible part of the electromagnetic spectrum of unintentionally doped ZnO NWs grown by chemical bath deposition (CBD) and annealed for 1 h under oxygen atmosphere in the temperature range of 200 to 1000 °C. The first data point is related to as-grown ZnO NWs.

Lorentzian function, as depicted in Fig. S6 in the Supplemental Material [60]. The evolution of the intensity of each visible emission band with annealing temperature is presented in logarithmic scale in Fig. 8. Both the red-orange and yellow-green emission bands exhibit a steady decrease in their relative intensity from the annealing temperatures of 200 to 400 °C, reaching an $\sim 64\%$ decrease at 400 °C. In contrast, the relative intensity of the green-blue emission band stabilizes at the annealing temperature of 200 °C after a significant drop and reaches an $\sim 54\%$ decrease at the annealing temperature of 400 °C. This steady decrease in the relative intensity of the visible emission bands in Fig. 8 is in very good agreement with the variation of the relative intensity of the Raman lines assigned to hydrogen-related defects in Fig. 4. At the annealing temperature of 500 °C, a general increase in the relative intensity of the visible emission bands correlates with the previously discussed broadening of the NBE emission, which appears to be due to the activation and generation processes of the $V_{Zn}-N_O-H$ defect complex. The thermal annealing at this temperature under oxygen atmosphere promotes the formation of N_O-H bonds [77] and could be accompanied with the formation of the $V_{Zn}-nH$ defect complex with a low coordination in the center and on the surfaces of ZnO NWs [37]. This can lead to the formation of the $V_{Zn}-N_O-H$ defect complex on the surfaces of ZnO NWs where holes are highly concentrated under electron beam excitation [14], leading to transition levels other than the expected $-1/-2$ one. This statement is very well supported by the largest increase in the relative intensity of the yellow-green emission band, which is related to the $+1/0$ and $0/-1$ transition levels of the $V_{Zn}-2H$ and $V_{Zn}-N_O-H$ defect complexes. The formation of the $V_{Zn}-N_O-H$ defect complex following a thermal annealing at 450 °C was also reported by Reynolds *et al.* [70]. Further thermal annealing from 600 to 900 °C shows that the red-orange and green-blue emission bands have a steady decrease in the relative intensity. In contrast, the yellow-green emission band presents a small

increase at the annealing temperatures of 700 and 900 °C, which is somehow in agreement with the evolution of the relative intensity of the Raman lines assigned to N_O-H bonds and the $V_{Zn}-N_O-H$ defect complex in Fig. 4. The red-orange and green-blue emission bands show a strong annihilation at the annealing temperature of 1000 °C, hence revealing the complete disappearance of $V_{Zn}-nH$ defect complexes, both in the bulk and on the surfaces of ZnO NWs, which is in accordance with the Raman spectra in Fig. 2. The yellow-green emission band also reveals a significant decrease in its relative intensity but not a complete annihilation, suggesting that the residual $V_{Zn}-N_O-H$ defect complex still occurs as further indicated by the less intense Raman line at 3078 cm^{-1} recorded after thermal annealing at 1000 °C.

E. Investigation of the LO phonon-plasmon coupled modes

Following the determination of the optical properties of as-grown and annealed ZnO NWs, their free charge carrier density and mobility were extracted by using Raman spectroscopy through the investigation of the coupling between the LO phonons and plasmons. When the LO phonon frequency is close to the free charge carrier plasmon frequency, their macroscopic electric fields strongly interact and couple, hence leading to the creation of LO phonon-plasmon (LPP) coupled modes. This methodology has been widely used in polar semiconductors and earlier reported for SiC and GaN bulk materials [90–92] and later for Si-doped GaN wires grown by metal-organic vapor phase epitaxy [93] and ZnO rods grown by chemical vapor deposition [94].

In as-grown and annealed ZnO NWs, their free charge carrier density (n) and mobility (μ) were evaluated via a line-shape fitting, in which both the contributions of the electro-optical mechanisms and of the deformation potential were considered [90]. The Raman scattering efficiency is then defined by the following equations:

$$I(\omega) \propto [1, C, C^2] \text{Im} \left[\frac{1}{\varepsilon(\omega)} \right],$$

and

$$\varepsilon(\omega) = \varepsilon_{\infty} \left[1 + \frac{\omega_{LO}^2 - \omega_{TO}^2}{\omega_{TO}^2 - \omega^2 - i\gamma\omega} - \frac{\omega_p^2}{\omega^2 + i\gamma_p\omega} \right],$$

where $\varepsilon(\omega)$ is the dielectric function, ω is the Raman shift, $\varepsilon_{\infty} = 3.68$ is the high-frequency dielectric constant of ZnO [95]. Here, $C = 6.4$ is the Faust-Henry constant [96], $\omega_{TO} = 409.7$ and $\omega_{LO} = 574.2\text{ cm}^{-1}$ are the frequencies for quasi-TO (qTO) and quasi-LO (qLO) phonon modes for ZnO NWs with a 6° vertical inclination [97,98]. For our LPP fitting model, the quasimodes were used as an optimization due to the vertical inclination of $5.8 \pm 4.5^\circ$ seen on the cross-sectional view FESEM images of spontaneously grown ZnO NWs in Fig. 1, which is close to the average 6° inclination angle previously reported in Ref. [55]. The phonon damping constant (γ) of the $A_1(LO)$ mode was assumed to be equal to the one of the nonpolar E_2^{high} mode, deduced from the FWHM of the E_2^{high} Raman line. The free charge carrier density can then be

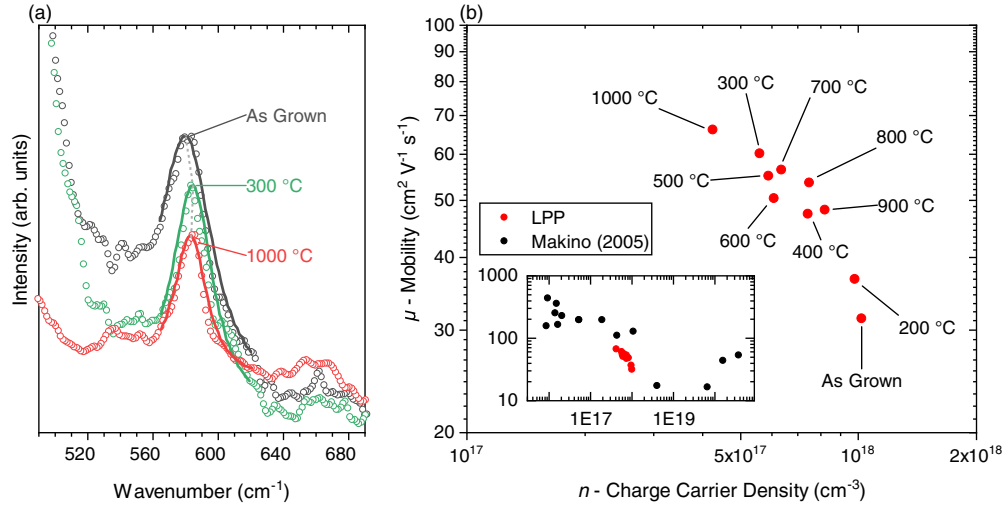


FIG. 9. (a) Theoretical calculation of the $A_1(\text{LO})$ phonon-plasmon intensity using optimized parameters reported in Table II for as-grown (black solid line), 300 °C (green solid line), and 1000 °C (red solid line) annealed ZnO NWs for 1 h under oxygen atmosphere. The empty circles represent the corresponding acquired Raman spectra for as-grown (black), 300 °C (green), and 1000 °C (red) annealed ZnO NWs for 1 h under oxygen atmosphere. (b) Mobility vs free charge carrier density (red dots) in as-grown and annealed ZnO NWs from 200 to 1000 °C as deduced from the best longitudinal optical phonon-plasmon (LPP) fit results. In the inset, Hall effect measurements for undoped and Ga-doped ZnO epitaxial thin films (black dots) are reported from Makino *et al.* [100] for comparison, along with the data of this paper (red dots).

determined by the plasmon frequency (ω_p) as follows:

$$\omega_p = \sqrt{\frac{4\pi e^2 n}{m^* \epsilon_\infty}},$$

and the mobility is linked to the plasmon damping constant (γ_p) as follows:

$$\gamma_p = \frac{e}{m^*(E_F)\mu},$$

where m^* is the effective mass of electrons in the parabolic, isotropic conduction band and equals $0.23 m_e$ at the Fermi level E_F [99]. As a result, the free charge carrier density and mobility are the only free parameters of the model.

The LPP fits for the $A_1(\text{LO})$ mode in as-grown, 300 and 1000 °C-annealed ZnO NWs are presented in Fig. 9(a). The model was evaluated over a wide range of free charge carrier density and mobility from 1.0×10^{16} to $3.1 \times 10^{19} \text{ cm}^{-3}$ and 1 to $150 \text{ cm}^2/\text{Vs}$, respectively, where the variation of the LPP fit from the $A_1(\text{LO})$ mode was calculated using a mean squared

error method. The related two-dimensional error color maps, where pairs of free charge carrier density and/or mobility values give a reliable fit with a root mean squared error < 0.05 , are shown in Fig. S7 in the Supplemental Material [60]. The best LPP fits for the $A_1(\text{LO})$ mode in as-grown and annealed ZnO NWs are shown in Fig. 9(b), along with the dedicated values for the fit parameters, as summarized in Table II.

The best LPP fit for as-grown ZnO NWs shows free charge carrier density and mobility values of $n = 1.02 \times 10^{18} \text{ cm}^{-3}$ and $\mu = 31.3 \text{ cm}^2/\text{Vs}$, respectively, corresponding to a resistivity value of $195.7 \text{ m}\Omega \text{ cm}$. Using four-point probe resistivity measurements in the patterned metal configuration, a free charge carrier density ranging from 2.7×10^{18} to 3.1×10^{19} and a resistivity ranging from 4.1 to $28.4 \text{ m}\Omega \text{ cm}$ were reported in as-grown ZnO NWs grown by CBD under the spontaneous growth approach using the same conditions [14]. The apparent discrepancy between the resistivity values obtained from the best LPP fit and four-point probe measurements in as-grown ZnO NWs is explained in detail in Fig. S8 in the Supplemental Material [60] and mainly originates from

TABLE II. (a) LPP fit parameters in as-grown and annealed ZnO NWs for 1 h under oxygen atmosphere in the temperature range of 200 to 1000 °C.

Sample	$A_1(\text{LO})$ peak position (cm^{-1})	$A_1(\text{LO})$ FWHM (cm^{-1})	ω_p (cm^{-1})	γ (cm^{-1})	γ_p (cm^{-1})	n ($\times 10^{17} \text{ cm}^{-3}$)	μ (cm^2/Vs)
As grown	581.2	31.2	328.3	5.3	1295.0	10.2	31.3
200	582.2	37.4	322.0	4.9	1106.0	9.8	36.7
300	584.6	23.6	243.7	4.1	674.0	5.6	60.2
400	584.6	34.1	280.7	4.7	856.0	7.4	47.4
500	584.0	34.7	250.0	4.6	736.0	5.9	55.2
600	583.5	28.4	253.7	4.7	804.0	6.1	50.5
700	585.3	32.2	259.6	4.6	718.0	6.4	56.5
800	587.0	38.9	281.6	4.5	756.0	7.5	53.7
900	585.2	51.5	295.1	4.6	843.0	8.2	48.2
1000	583.3	27.2	212.3	4.2	613.0	4.3	66.2

the oxygen species adsorbed on the NW surfaces during the Raman scattering measurement. It was shown in Ref. [14] that the NWs exhibit a metallic bulklike electrical conduction dominated by the core. When probing an array of NWs by Raman scattering, an average LPP coupling is obtained due to the contributions from the core of the NW representing a flat-band regime and the surface-depleted region of the NW representing an upward band-bending regime [89], where the free charge carrier density is considerably lower than in the bulk section due to the adsorbed oxygen species on the NW surfaces. Four-point probe resistivity measurements show a sudden increase in the resistivity of the NW due to its exposure to air. Resistivity values in as-grown ZnO NWs suddenly exposed to ambient conditions rise from 70.3 to 100.3 mΩ cm, which fall in closer correlation with the 195.7 mΩ cm resistivity value obtained from the best LPP fit. The mobility values fall in the range of 31.3 to 66.2 cm²/Vs, which is in very good agreement with the typical values reported from FET measurements [101,102]. The smallest free charge carrier density of $n = 4.3 \times 10^{17} \text{ cm}^{-3}$ together with the largest mobility of $\mu = 66.2 \text{ cm}^2/\text{Vs}$ are obtained in ZnO NWs annealed at the highest temperature of 1000 °C, where the concentration of nitrogen- and hydrogen-related defects is by far the smallest one in the series of samples. It is worth noticing that the second smallest free carrier density of $n = 5.6 \times 10^{17} \text{ cm}^{-3}$ and the second largest mobility of $\mu = 60.2 \text{ cm}^2/\text{Vs}$ are obtained in ZnO NWs annealed at the relatively low temperature of 300 °C, where the nitrogen-related defects exhibit one of the highest concentrations.

F. Effects of thermal annealing on nitrogen- and hydrogen-related defects

The effects of thermal annealing under oxygen atmosphere on the nature of nitrogen- and hydrogen-related defects in unintentionally doped ZnO NWs by CBD are summarized in Fig. 10. The schematic illustration consists of an inclined top-view cross-section of one ZnO NW, where spheres represent single point defects and their association to form the nitrogen- and hydrogen-related defects distributed along the profile of the NW. It aims at representing the different mechanisms of reaction at work during thermal annealing at different temperatures from 200 to 1000 °C. The involvement of hydrogen, carbon, and nitrogen species along with their association gives rise to many nitrogen- and hydrogen-related defects with different characteristics, as recapitulated in Table III.

The as-grown ZnO NWs show the presence of relevant and well-known hydrogen-related defects, including H_{BC}, the V_{Zn}-nH defect complex with $n = 1-3$, C-H_x, and N_O-H bonds [14], along with the V_{Zn}-N_O-H defect complex.

Following thermal annealing at the low temperature of 200 °C, a strong reduction of H_{BC} occurs, indicating the formation of electrically inactive H₂ molecules [Fig. 10(2a)] [34], which can either be trapped in the center of ZnO NWs or exodiffuse if located nearby their surfaces [Fig. 10(2b)]. The N_O-H defect complexes are also affected strongly, and their concentration is significantly reduced as well as the V_{Zn}-N_O-H defect complex but to a much smaller extent. Further thermal annealing at 300 °C results in the dissociation of H₂ molecules and makes energetically more favorable H_i [Fig. 10(3a)] [34],

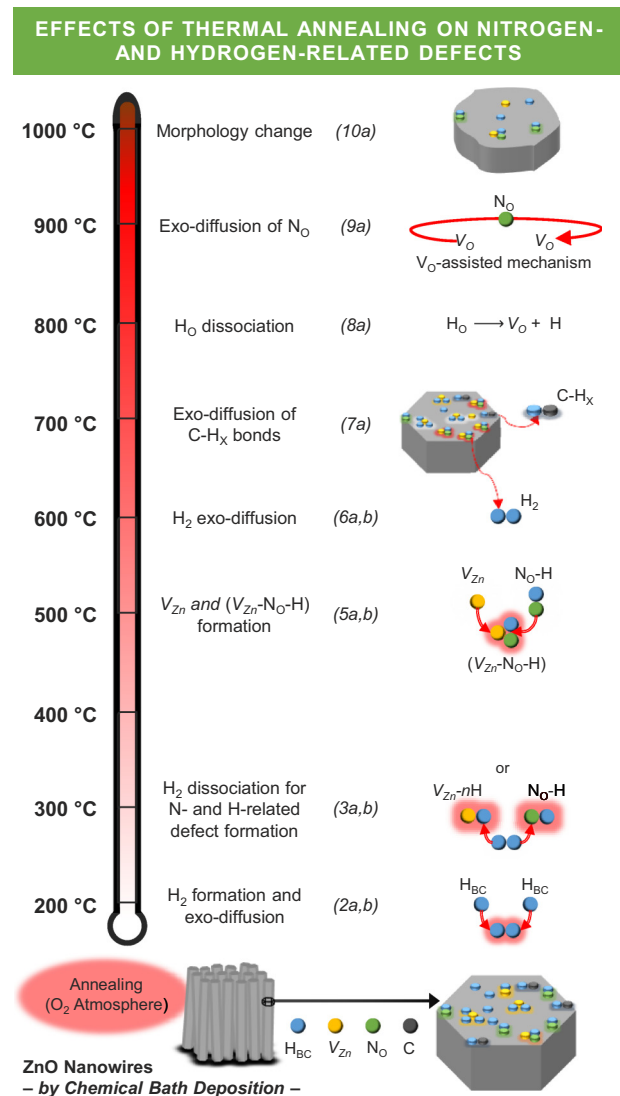


FIG. 10. Schematic illustration depicting the different mechanisms of reaction of nitrogen- and hydrogen-related defects at different annealing temperatures under oxygen atmosphere. (2a,b) Formation of H₂ molecules from two H_{BC} defects and exodiffusion of H₂ molecules at 200 °C. (3a,b) At 300 °C, H₂ molecules dissociate back into the H_{BC} defect and preferentially form other nitrogen- and hydrogen-related defects. (5a,b) At 500 °C, V_{Zn} is formed and reacts with the N_O-H groups to create the V_{Zn}-N_O-H defect complex. (6a) Exodiffusion of H_{BC} defects through the formation of H₂ molecules; (6b) Further activation and generation of the V_{Zn}-N_O-H defect complex similarly to (5b). (7a) Exodiffusion of C-H_x bonds at 700 °C. (8a) Dissociation of H₂O and the related formation of V₀ and H_{BC} at 800 °C. (9a) At 900 °C, N_O atoms exodiffuse via a V₀-assisted mechanism through the formation of N₂ molecules. (10a) At 1000 °C, a morphology change is induced, and the hexagonal shape is lost. Note: the main nitrogen- and hydrogen-related defects are represented via the association of spheres representing single point defects for illustration purposes, hence no real scale is presented here.

which can either rest as H_{BC} or be preferentially trapped by other nitrogen- and hydrogen-related defects to form the V_{Zn}-nH defect complexes with $n = 1-3$ and N_O-H groups [Fig. 10(3b)]. It appears that the free charge carrier density in

TABLE III. Recapitulating characteristics of the main nitrogen- and hydrogen-related defects with their respective infrared/Raman lines, E_{emission} in luminescence spectroscopy using DFT calculations, and photoluminescence/cathodoluminescence lines.

	Infrared/Raman modes (cm ⁻¹)		E_{emission} (eV)		Photoluminescence/cathodoluminescence (eV)
H _{BC}	330/3611 ^{a,b,c}	–	–	–	3.3601 ^c
H _O	273 ^d	–	–	–	3.3628 (I ₄) ^c
V _{Zn}	–	$\varepsilon(+2/+1)$	2.53 ^e	2.40 ^f	1.60 ^{g,h}
		$\varepsilon(+1/0)$	2.48 ^e	1.90 ^f	
		$\varepsilon(0/-1)$	2.19 ^e	1.29 ^f	
		$\varepsilon(-1/-2)$	1.60 ^e	0.78 ^f	
V _{Zn} -H	3306–3418 ^{a,f}	$\varepsilon(+2/+1)$	2.49 ^e	2.35 ^f /2.46 ⁱ	–
		$\varepsilon(+1/0)$	2.40 ^e	1.96 ^f /1.81 ⁱ	
		$\varepsilon(0/-1)$	1.82 ^e	1.31 ^f /1.30 ⁱ	
V _{Zn} -2H	3312/3349 ^a	$\varepsilon(+2/+1)$	2.46 ^e	2.30 ^f	–
		$\varepsilon(+1/0)$	2.29 ^e	2.08 ^f /1.84 ⁱ	
V _{Zn} -3H	3303/3321 ^j	$\varepsilon(+1/0)$	3.37 ^e	–	3.36143 (I ₅) ^k
N _O -H (AB _{N⊥})	3055 ^l /3121 ^m	–	–	–	–
N _O -H (AB _N)	3084 ^l /3150 ^{n,o} /3160 ^m	–	–	–	–
V _{Zn} -N _O -H	3078 ^{p,m}	$\varepsilon(+1/0)$	2.50 ^m	–	–
		$\varepsilon(0/-1)$	2.27 ^m	–	–
		$\varepsilon(-1/-2)$	1.82 ^m	–	–
C-H _x	2890, 2918, 2988 ^q	–	–	–	–
O-H	3500 ^{a,p}	–	–	–	–

^aReference [24].

^bReference [74].

^cReference [25].

^dReference [34].

^eReference [14] (GGA + U approach).

^fReference [53] (hybrid functionals).

^gReference [104].

^hReference [105].

ⁱReference [54] (hybrid functionals).

^jReference [76].

^kReference [27].

^lReference [39].

^mThis paper (GGA + U approach).

ⁿReference [40].

^oReference [69].

^pReference [70].

^qReference [38].

ZnO NWs is significantly reduced here and reaches the second smallest value. This is due to the redistribution of the nitrogen- and hydrogen-related defects, for which the nature differs and involves shallow donors and deep acceptors. These behaviors have clearly been shown and discussed in the framework of Figs. 3 and 7.

Following thermal annealing at 500 °C, the activation and generation of the V_{Zn}-N_O-H defect complex with the –2 charge state is revealed through the formation of V_{Zn} at high temperatures [Fig. 10(5a)] and its reaction with the N_O-H groups [Fig. 10(5b)]. The broadening of the NBE emission in the cathodoluminescence spectrum along with the sharp increase in the relative intensity of the green-blue emission band are strong evidence [70,77,103]. At the annealing temperature of 600 °C, an exodiffusion phenomenon of H_{BC} in the form of H₂ molecules is expected to some extent [Fig. 10(6a)], together with the further activation and generation of the V_{Zn}-N_O-H defect complex [Fig. 10(6b)]. The important contribution of the V_{Zn}-N_O-H defect complex

through the predominance of A°X_A transitions in the NBE emission is strong evidence [70]. Further annealing in the range of 700 to 900 °C results in an interplay between the activation, and formation of the V_{Zn}-N_O-H defect complex, owing to the observed A°X_A [83,84], DAP [85–87], and FA [88] transitions, as typically reported in nitrogen-doped ZnO films and NWs. Additionally, the vanishing of C–H_x bonds trapped on the m -plane sidewalls of ZnO NWs is activated from the annealing temperature of 700 °C [Fig. 10(7a)].

The exodiffusion phenomenon of N_O located in the bulk of ZnO at high annealing temperature has been proposed via an oxygen vacancy-assisted mechanism [78]. High temperature annealing under oxygen atmosphere is not favorable to the formation of oxygen vacancies, but the contribution of H_O should be considered here as its presence has already been noticed in ZnO nanorods grown by CBD with the same conditions [13]. Given that H_O is stable up to 800 °C [34], the high annealing temperatures could dissociate H_O and lead to its exodiffusion, in turn leaving oxygen vacancies [Fig. 10(8a)] that

could be involved in the suggested oxygen vacancy-assisted mechanism. The dissociation of nitrogen-related defects along with the oxygen vacancy-assisted mechanism [Fig. 10(9a)] and further binding of two interstitial nitrogen atoms would form a N_2 molecule [78], hence deactivating N_O . Finally, the thermal annealing at 1000 °C shows a clear morphology change where the hexagonal shape is lost [Fig. 10(10a)] and a strong decrease in the concentration of hydrogen-related defects is inferred, but the nitrogen-related defects still occur to some extent. The annihilation of the related visible emission bands is strong evidence. Interestingly, the clear NBE emission related to H_O via the I_4 line and its related TES shoulder at 1000 °C give an insight into its presence in ZnO NWs grown by CBD. Hence, correlating these findings, it can be stated that residual H_O , H_{BC} , V_{Zn} , N_O -H bonds, and the V_{Zn} - N_O -H defect complex are expected at 1000 °C, while the V_{Zn} - nH defect complexes with $n = 1-3$ have completely vanished. It appears that the free charge carrier density is significantly decreased and reaches the smallest value of the series of samples.

IV. CONCLUSIONS

In summary, we have shown that the nitrogen- and hydrogen-related defects represent the major source of crystal defects in unintentionally doped ZnO NWs grown by CBD owing to the large number of impurities contained in a growth medium. In addition to H_{BC} , H_O , and V_{Zn} - nH defect complexes, the nitrogen-related defects including N_O -H and V_{Zn} - N_O -H defect complexes also strongly affect the physical properties of ZnO NWs. The V_{Zn} - N_O -H defect complex acts as a deep acceptor with a relatively low formation energy and exhibits a prominent Raman line at 3078 cm^{-1} along with a red-orange emission energy of ~ 1.82 eV in cathodoluminescence spectroscopy. The N_O -H bonds in $AB_{N\perp}$ and

$AB_{N\parallel}$ configurations further lead to two Raman lines at 3121 and 3160 cm^{-1} , respectively. The tuning of the nitrogen- and hydrogen-related defects has been achieved using thermal annealing under oxygen atmosphere, resulting in a rather complex, fine evolution of their nature and concentration as a function of annealing temperature ranging from 200 to 1000 °C. Their resulting electrical properties significantly depend on the balance between the nitrogen- and hydrogen-related defects and on their redistribution upon thermal annealing. ZnO NWs annealed at the moderate temperature of 300 °C specifically exhibit one of the smallest free charge carrier densities of $5.6 \times 10^{17} cm^{-3}$ along with a high mobility of $\sim 60 cm^2/Vs$ following the analysis of LPP coupling. A comprehensive diagram showing the complex interplay of each nitrogen- and hydrogen-related defect during thermal annealing and its dependence on the annealing temperature has been gained. Eventually, the engineering of the nitrogen- and hydrogen-related defects as the major source of crystal defects in unintentionally doped ZnO NWs grown by CBD is capital to control their electronic structure properties governing their electrical and optical properties in any nanoscale engineering devices.

ACKNOWLEDGMENTS

The authors are grateful for the financial support from the French National Research Agency through the project ROLLER (ANR-17-CE09-0033). J.V. held a doctoral fellowship from the ROLLER project. This research further benefited from some of the characterization equipment of the Grenoble INP-CMTC platform as well as from CIMENT/GRICAD platform in Grenoble for computational resources. It was also supported by computational time granted from the Greek Research & Technology Network (GRNET) in the ARIS National HPC infrastructure under the project AIMONACA (pr008002).

-
- [1] Z. L. Wang, *Adv. Funct. Mater.* **18**, 3553 (2008).
 - [2] V. Consonni, and A. M. Lord, *Nano Energy* **83**, 105789 (2021).
 - [3] C. F. Pan, J. Y. Zhai, and Z. L. Wang, *Chem. Rev.* **119**, 9303 (2019).
 - [4] M. Willander *et al.*, *Nanotechnology* **20**, 332001 (2009).
 - [5] V. Consonni, J. Briscoe, E. Karber, X. Li, and T. Cossuet, *Nanotechnology* **30**, 362001 (2019).
 - [6] S. Rackauskas, N. Barbero, C. Barolo, and G. Viscardi, *Nanomaterials* **7**, 381 (2017).
 - [7] L. Vayssieres, *Adv. Mater.* **15**, 464 (2003).
 - [8] K. M. McPeak, M. A. Becker, N. G. Britton, H. Majidi, B. A. Bunker, and J. B. Baxter, *Chem. Mater.* **22**, 6162 (2010).
 - [9] J. J. Cheng, S. M. Nicaise, K. K. Berggren, and S. Gradecak, *Nano Lett.* **16**, 753 (2016).
 - [10] C. Lausecker, B. Salem, X. Baillin, and V. Consonni, *J. Phys. Chem. C* **123**, 29476 (2019).
 - [11] X. H. Huang, Z. Y. Zhan, K. P. Pramoda, C. Zhang, L. X. Zheng, and S. J. Chua, *CrystEngComm* **14**, 5163 (2012).
 - [12] E. G. Barbagiovanni, R. Reitano, G. Franzo, V. Strano, A. Terrasi, and S. Mirabella, *Nanoscale* **8**, 995 (2016).
 - [13] T. Cossuet, F. Donatini, A. M. Lord, E. Appert, J. Pernot, and V. Consonni, *J. Phys. Chem. C* **122**, 22767 (2018).
 - [14] J. Villafuerte, F. Donatini, J. Kioseoglou, E. Sarigiannidou, O. Chaix-Pluchery, J. Pernot, and V. Consonni, *J. Phys. Chem. C* **124**, 16652 (2020).
 - [15] J. B. Baxter, and C. A. Schmuttenmaer, *J. Phys. Chem. B* **110**, 25229 (2006).
 - [16] A. M. Lord, T. G. Maffei, A. S. Walton, D. M. Kepaptsoglou, Q. M. Ramasse, M. B. Ward, J. Koble, and S. P. Wilks, *Nanotechnology* **24**, 435706 (2013).
 - [17] C. Opoku, A. S. Dahiya, F. Cayrel, G. Poulin-Vittrant, D. Alquier, and N. Camara, *RSC Adv.* **5**, 69925 (2015).
 - [18] L. Wang, S. Guillemin, J. M. Chauveau, V. Sallet, F. Jomard, R. Brenier, V. Consonni, and G. Bremond, *Phys. Status Solidi C* **13**, 576 (2016).
 - [19] C. G. Van de Walle, *Phys. Rev. Lett.* **85**, 1012 (2000).
 - [20] A. Janotti, and C. G. Van de Walle, *Nat. Mater.* **6**, 44 (2007).
 - [21] M. G. Wardle, J. P. Goss, and P. R. Briddon, *Phys. Rev. B* **72**, 155108 (2005).
 - [22] S. Z. Karazhanov, E. S. Marstein, and A. Holt, *J. Appl. Phys.* **105**, 033712 (2009).

- [23] D. M. Hofmann, A. Hofstaetter, F. Leiter, H. J. Zhou, F. Henecker, B. K. Meyer, S. B. Orlinskii, J. Schmidt, and P. G. Baranov, *Phys. Rev. Lett.* **88**, 045504 (2002).
- [24] E. V. Lavrov, J. Weber, F. Bornert, C. G. Van de Walle, and R. Helbig, *Phys. Rev. B* **66**, 165205 (2002).
- [25] E. V. Lavrov, F. Herklotz, and J. Weber, *Phys. Rev. B* **79**, 165210 (2009).
- [26] B. K. Meyer, H. Alves, D. M. Hofmann, W. Kriegseis, D. Forster, F. Bertram, J. Christen, A. Hoffmann, M. Strassburg, M. Dworzak, U. Habocek, and A. V. Rodina, *Phys. Status Solidi B* **241**, 231 (2004).
- [27] R. Heinhold, A. Neiman, J. V. Kennedy, A. Markwitz, R. J. Reeves, and M. W. Allen, *Phys. Rev. B* **95**, 054120 (2017).
- [28] Y. Gao, and Z. L. Wang, *Nano Lett.* **9**, 1103 (2009).
- [29] G. Romano, G. Mantini, A. Di Carlo, A. D'Amico, C. Falconi, and Z. L. Wang, *Nanotechnology* **22**, 465401 (2011).
- [30] R. Hinchet, S. Lee, G. Ardila, L. Montes, M. Mouis, and Z. L. Wang, *Adv. Funct. Mater.* **24**, 971 (2014).
- [31] G. Tian, D. Xiong, Y. Su, T. Yang, Y. Gao, C. Yan, W. Deng, L. Jin, H. Zhang, X. Fan, C. Wang, W. Deng, and W. Yang, *Nano Lett.* **20**, 4270 (2020).
- [32] J. I. Sohn, S. N. Cha, B. G. Song, S. Lee, S. M. Kim, J. Ku, H. J. Kim, Y. J. Park, B. L. Choi, Z. L. Wang, J. M. Kim, and K. Kim, *Energy Environ. Sci.* **6**, 97 (2013).
- [33] R. Tao, M. Mouis, and G. Ardila, *Adv. Electron. Mater.* **4**, 1700299 (2018).
- [34] S. G. Koch, E. V. Lavrov, and J. Weber, *Phys. Rev. B* **89**, 235203 (2014).
- [35] X. H. Huang, C. B. Tay, Z. Y. Zhan, C. Zhang, L. X. Zheng, T. Venkatesan, and S. J. Chua, *Crystengcomm* **13**, 7032 (2011).
- [36] Z. N. Urgessa, J. R. Botha, M. O. Eriksson, C. M. Mbulanga, S. R. Dobson, S. R. Tankio Djiokap, K. F. Karlsson, V. Khranovskyy, R. Yakimova, and P. O. Holtz, *J. Appl. Phys.* **116**, 123506 (2014).
- [37] A. M. Lord, V. Consonni, T. Cossuet, F. Donatini, and S. P. Wilks, *ACS Appl. Mater. Interfaces* **12**, 13217 (2020).
- [38] N. H. Nickel, and K. Fleischer, *Phys. Rev. Lett.* **90**, 197402 (2003).
- [39] X. N. Li, B. Keyes, S. Asher, S. B. Zhang, S. H. Wei, T. J. Coutts, S. Limpijumngong, and C. G. Van de Walle, *Appl. Phys. Lett.* **86**, 122107 (2005).
- [40] S. J. Jokela, and M. D. McCluskey, *Phys. Rev. B* **76**, 193201 (2007).
- [41] S. J. Jokela, and M. D. McCluskey, *J. Appl. Phys.* **107**, 113536 (2010).
- [42] P. E. Blochl, *Phys. Rev. B* **50**, 17953 (1994).
- [43] G. Kresse, and D. Joubert, *Phys. Rev. B* **59**, 1758 (1999).
- [44] J. P. Perdew, K. Burke, and M. Ernzerhof, *Phys. Rev. Lett.* **77**, 3865 (1996).
- [45] J. P. Perdew, K. Burke, and M. Ernzerhof, *Phys. Rev. Lett.* **78**, 1396(E) (1997).
- [46] K. Harun, N. A. Salleh, B. Deghfel, M. K. Yaakob, and A. A. Mohamad, *Results Phys.* **16**, 102829 (2020).
- [47] N. N. Lathiotakis, A. N. Andriotis, and M. Menon, *Phys. Rev. B* **78**, 193311 (2008).
- [48] R. M. Sheetz, I. Ponomareva, E. Richter, A. N. Andriotis, and M. Menon, *Phys. Rev. B* **80**, 195314 (2009).
- [49] K. J. May, and A. M. Kolpak, *Phys. Rev. B* **101**, 165117 (2020).
- [50] I. S. Elfimov, A. Rusydi, S. I. Csiszar, Z. Hu, H. H. Hsieh, H. J. Lin, C. T. Chen, R. Liang, and G. A. Sawatzky, *Phys. Rev. Lett.* **98**, 137202 (2007).
- [51] S. S. Parhizgar, and J. Beheshtian, *Computational Condens. Matter* **15**, 1 (2018).
- [52] A. Janotti, and C. G. Van de Walle, *Rep. Prog. Phys.* **72**, 126501 (2009).
- [53] J. L. Lyons, J. B. Varley, D. Steiauf, A. Janotti, and C. G. Van de Walle, *J. Appl. Phys.* **122**, 035704 (2017).
- [54] Y. K. Frodason, K. M. Johansen, T. S. Bjorheim, B. G. Svensson, and A. Alkauskas, *Phys. Rev. B* **97**, 104109 (2018).
- [55] S. Guillemin, E. Appert, H. Roussel, B. Doisneau, R. Parize, T. Boudou, G. Bremond, and V. Consonni, *J. Phys. Chem. C* **119**, 21694 (2015).
- [56] R. Parize, J. Garnier, O. Chaix-Pluchery, C. Verrier, E. Appert, and V. Consonni, *J. Phys. Chem. C* **120**, 5242 (2016).
- [57] S. Guillemin, V. Consonni, E. Appert, E. Puyoo, L. Rapenne, and H. Roussel, *J. Phys. Chem. C* **116**, 25106 (2012).
- [58] G. Guisbiers, and S. Pereira, *Nanotechnology* **18**, 435710 (2007).
- [59] S. Guillemin, E. Sarigiannidou, E. Appert, F. Donatini, G. Renou, G. Bremond, and V. Consonni, *Nanoscale* **7**, 16994 (2015).
- [60] See Supplemental Material at <http://link.aps.org/supplemental/10.1103/PhysRevMaterials.5.056001> for Raman spectra with a zoom-in of the area of interest at high wavenumber, evolution of the position and FWHM of the E_2^{high} Raman line vs annealing temperature, DOS of the $V_{\text{Zn}}\text{-N}_\text{O}\text{-H}$ defect complex vs energy, evolution of the position and FWHM of the NBE emission vs annealing temperature, evolution of the acceptor-to-donor ratio (i.e., $V_{\text{Zn}}\text{-N}_\text{O}\text{-H}$ to H_{BC}) vs annealing temperature, deconvolution of the visible emission bands in a typical cathodoluminescence spectrum, theoretical calculations of the $A_1(\text{LO})$ phonon-plasmon intensity, I - V measurements using a four-point probe device, and four-point probe resistance to length ratio vs electron beam dose.
- [61] R. Cusco, E. Alarcon-Llado, J. Ibanez, L. Artus, J. Jimenez, B. G. Wang, and M. J. Callahan, *Phys. Rev. B* **75**, 165202 (2007).
- [62] C. Bundesmann, N. Ashkenov, M. Schubert, D. Spemann, T. Butz, E. M. Kaidashev, M. Lorenz, and M. Grundmann, *Appl. Phys. Lett.* **83**, 1974 (2003).
- [63] C. Verrier, E. Appert, O. Chaix-Pluchery, L. Rapenne, Q. Raffhay, A. Kaminski-Cachopo, and V. Consonni, *Inorg. Chem.* **56**, 13111 (2017).
- [64] P. Gaffuri, E. Appert, O. Chaix-Pluchery, L. Rapenne, M. Salaun, and V. Consonni, *Inorg. Chem.* **58**, 10269 (2019).
- [65] A. Kaschner, U. Habocek, M. Strassburg, M. Strassburg, G. Kraczmarczyk, A. Hoffmann, C. Thomsen, A. Zeuner, H. R. Alves, D. M. Hofmann, and B. K. Meyer, *Appl. Phys. Lett.* **80**, 1909 (2002).
- [66] A. Sugunan, H. C. Warad, M. Boman, and J. Dutta, *J. Sol-Gel Sci. Techn.* **39**, 49 (2006).
- [67] V. Strano, R. G. Urso, M. Scuderi, K. O. Iwu, F. Simone, E. Ciliberto, C. Spinella, and S. Mirabella, *J. Phys. Chem. C* **118**, 28189 (2014).
- [68] J. Hu, H. Y. He, and B. C. Pan, *J. Appl. Phys.* **103**, 113706 (2008).
- [69] O. S. Kumar, E. Watanabe, R. Nakai, N. Nishimoto, and Y. Fujita, *J. Cryst. Growth* **298**, 491 (2007).

- [70] J. G. Reynolds, C. L. Reynolds, A. Mohanta, J. F. Muth, J. E. Rowe, H. O. Everitt, and D. E. Aspnes, *Appl. Phys. Lett.* **102**, 152114 (2013).
- [71] L. Liu *et al.*, *Phys. Rev. Lett.* **108**, 215501 (2012).
- [72] M. N. Amini, R. Saniz, D. Lamoén, and B. Partoens, *Phys. Chem. Chem. Phys.* **17**, 5485 (2015).
- [73] D. Y. Yong, H. Y. He, Z. K. Tang, S. H. Wei, and B. C. Pan, *Phys. Rev. B* **92**, 235207 (2015).
- [74] E. V. Lavrov, F. Bornert, and J. Weber, *Phys. Rev. B* **71**, 035205 (2005).
- [75] E. V. Lavrov, *Physica B* **340-342**, 195 (2003).
- [76] F. Herklotz, A. Hupfer, K. M. Johansen, B. G. Svensson, S. G. Koch, and E. V. Lavrov, *Phys. Rev. B* **92**, 155203 (2015).
- [77] J. Y. Gao, X. Z. Zhang, Y. H. Sun, Q. Zhao, and D. P. Yu, *Nanotechnology* **21**, 245703 (2010).
- [78] J. Y. Gao, R. Qin, G. F. Luo, J. Lu, Y. Leprince-Wang, H. Q. Ye, Z. M. Liao, Q. Zhao, and D. P. Yu, *Phys. Lett. A* **374**, 3546 (2010).
- [79] M. G. Wardle, J. P. Goss, and P. R. Briddon, *Phys. Rev. Lett.* **96**, 205504 (2006).
- [80] U. Herath, P. Tavazde, X. He, E. Bousquet, S. Singh, F. Muñoz, and A. H. Romero, *Comput. Phys. Commun.* **251**, 107080 (2020).
- [81] A. Teke, U. Ozgur, S. Dogan, X. Gu, H. Morkoc, B. Nemeth, J. Nause, and H. O. Everitt, *Phys. Rev. B* **70**, 195207 (2004).
- [82] Y. G. Wang, S. P. Lau, H. W. Lee, S. F. Yu, B. K. Tay, X. H. Zhang, and H. H. Hng, *J. Appl. Phys.* **94**, 354 (2003).
- [83] D. C. Look, D. C. Reynolds, C. W. Litton, R. L. Jones, D. B. Eason, and G. Cantwell, *Appl. Phys. Lett.* **81**, 1830 (2002).
- [84] X. D. Yang, Z. Y. Xu, Z. Sun, B. Q. Sun, L. Ding, F. Z. Wang, and Z. Z. Ye, *J. Appl. Phys.* **99**, 046101 (2006).
- [85] J. F. Rommeluere, L. Svob, F. Jomard, J. Mimila-Arroyo, A. Lusson, V. Sallet, and Y. Marfaing, *Appl. Phys. Lett.* **83**, 287 (2003).
- [86] D. Pfisterer, J. Sann, D. M. Hofmann, M. Plana, A. Neumann, M. Lerch, and B. K. Meyer, *Phys. Status Solidi B* **243**, R1 (2006).
- [87] B. P. Zhang, N. T. Binh, Y. Segawa, K. Wakatsuki, and N. Usami, *Appl. Phys. Lett.* **83**, 1635 (2003).
- [88] J. W. Sun, Y. M. Lu, Y. C. Liu, D. Z. Shen, Z. Z. Zhang, B. Yao, B. H. Li, J. Y. Zhang, D. X. Zhao, and X. W. Fan, *J. Appl. Phys.* **102**, 043522 (2007).
- [89] C. Soci, A. Zhang, B. Xiang, S. A. Dayeh, D. P. R. Aplin, J. Park, X. Y. Bao, Y. H. Lo, and D. Wang, *Nano Lett.* **7**, 1003 (2007).
- [90] H. Harima, S. Nakashima, and T. Uemura, *J. Appl. Phys.* **78**, 1996 (1995).
- [91] T. Kozawa, T. Kachi, H. Kano, Y. Taga, M. Hashimoto, N. Koide, and K. Manabe, *J. Appl. Phys.* **75**, 1098 (1994).
- [92] P. Perlin, J. Camassel, W. Knap, T. Taliercio, J. C. Chervin, T. Suski, I. Grzegory, and S. Porowski, *Appl. Phys. Lett.* **67**, 2524 (1995).
- [93] P. Tchouffian, F. Donatini, F. Levy, B. Amstatt, A. Dussaigne, P. Ferret, E. Bustarret, and J. Pernot, *Appl. Phys. Lett.* **103**, 202101 (2013).
- [94] A.-J. Cheng, Y. Tzeng, H. Xu, S. Alur, Y. Wang, M. Park, T.-H. Wu, C. Shannon, D.-J. Kim, and D. Wang, *J. Appl. Phys.* **105**, 073104 (2009).
- [95] H. Yoshikawa, and S. Adachi, *Jpn. J. Appl. Phys.* **36**, 6237 (1997).
- [96] B. H. Bairamov, A. Heinrich, G. Irmer, V. V. Toporov, and E. Ziegler, *Phys. Status Solidi B* **119**, 227 (1983).
- [97] R. Loudon, *Adv. Phys.* **50**, 813 (2001).
- [98] T. Cossuet, H. Roussel, J. M. Chauveau, O. Chaix-Pluchery, J. L. Thomassin, E. Appert, and V. Consonni, *Nanotechnology* **29**, 475601 (2018).
- [99] M. Oshikiri, Y. Imanaka, F. Aryasetiawan, and G. Kido, *Physica B* **298**, 472 (2001).
- [100] T. Makino, Y. Segawa, A. Tsukazaki, A. Ohtomo, and M. Kawasaki, *Appl. Phys. Lett.* **87**, 022101 (2005).
- [101] W. I. Park, J. S. Kim, G. C. Yi, M. H. Bae, and H. J. Lee, *Appl. Phys. Lett.* **85**, 5052 (2004).
- [102] D. Kalblein, R. T. Weitz, H. J. Bottcher, F. Ante, U. Zschieschang, K. Kern, and H. Klauk, *Nano Lett.* **11**, 5309 (2011).
- [103] R. Kobayashi, T. Kishi, Y. Katayanagi, T. Yano, and N. Matsushita, *RSC Adv.* **8**, 23599 (2018).
- [104] X. J. Wang, L. S. Vlasenko, S. J. Pearton, W. M. Chen, and I. A. Buyanova, *J. Phys. D: Appl. Phys.* **42**, 175411 (2009).
- [105] Y. Dong, F. Tuomisto, B. G. Svensson, A. Y. Kuznetsov, and L. J. Brillson, *Phys. Rev. B* **81**, 081201(R) (2010).